ACS APPLIED ELECTRONIC MATERIALS

pubs.acs.org/acsaelm Article

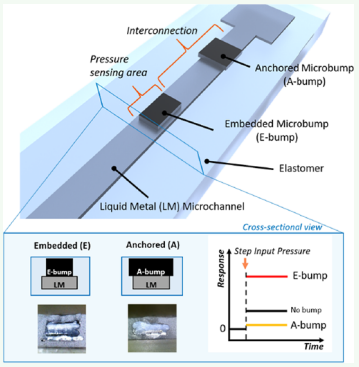
Sensitivity-Controllable Liquid-Metal-Based Pressure Sensor for Wearable Applications

Osman Gul,[#] Kyuyoung Kim,[#] Jimin Gu, Jungrak Choi, Dionisio Del Orbe Henriquez, Junseong Ahn, and Inkyu Park*

Cite This: *ACS Appl. Electron. Mater.* 2021, 3, 4027−4036 Read Online

ACCESS | Metrics & More | Article Recommendations | Supporting Information

ABSTRACT: Liquid-metal-based sensors have great opportunities in various applications such as health monitoring, intelligent artificial skin, and soft robotics. However, current liquid-metal-based pressure sensors suffer from low pressure sensitivity, low signal reliability, and poor interconnection properties. This paper introduces a sensitivity-engineerable, reliable liquid-metal-based pressure sensor with a robust interconnection structure for multifunctional wearable applications. Herein, we investigated the effects of dimensions of rigid microbumps on the liquid-metal-based soft pressure sensor. Furthermore, two different types of rigid microbump structures such as embedded bump (E-bump) and anchored bump (A-bump) were designed and integrated with a liquid metal microchannel using multimaterial 3D printing technology, and it enabled the engineering of pressure sensitivity for different purposes. High sensitivity was achieved with E-bump structures, and a robust interconnection structure was realized with A-bump structures. Integration of E-bumps has increased the average sensitivity of the sensor to 0.0727 kPa^{-1} (5.43 times higher), and A-bump integration has decreased the average sensitivity to 0.0004 Pa^{-1} (91.65 times lower) in the range of 0−50 kPa, as compared to the pressure sensor without any microbumps. Therefore, the liquid metal interconnection was established with the A-bump structures for reliable pressure monitoring in practical wearable applications. These characteristics allow the demonstration of the multifunctional wearable electronic applications, including a fingertip pressure sensor glove for wireless multiposition wrist pulse monitoring as traditional East Asian medicine pulse diagnosis and a wireless human−machine interface device.

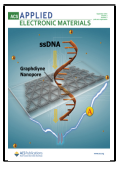


KEYWORDS: *liquid metal, 3D printing, wearable sensors, health monitoring, human pulse diagnosis, human−machine interface*

INTRODUCTION

Wearable pressure sensors are under tremendously high demand of improvement due to their diverse applications such as mobile healthcare, entertainment, and virtual/augmented reality systems. In contrast to conventional sensors, wearable pressure sensors need to satisfy several requirements such as high sensitivity, high flexibility, wearability, signal stability, lightweight, and low cost. Various attempts have been made to fulfill these requirements, specifically to increase the sensitivity of the wearable pressure sensors. To increase the pressure sensitivity, elastomers and a wide range of functional materials such as graphene,[1−4] carbon black,[5−7] nanowires,[8,9] and nanoparticles[10,11] have been utilized, which can be classified as solid-state pressure sensors. These sensors have suffered from long-term instability, limited stretchability, and signal drifting due to the difference in mechanical properties between the flexible substrate and functional sensing materials. Therefore, liquid-state sensors based on liquid metals and ionic liquids have been proposed to overcome the limitations of solid-state sensors for wearable electronic applications. In particular, the stretchability of liquid state sensors is less limited due to the utilization of liquid electrodes as the sensing materials. Due to negligible friction at the interface of liquid and the encapsulating elastomer, the characteristics of liquid electrodes are not degraded by harsh mechanical loadings. Ionic liquids have a high degree of freedom in the engineered material properties using diverse chemicals such as salts in the liquid or gel state. Therefore, the ionic liquid-based pressure sensors can have high-pressure sensitivity. However, they suffer from poor electrochemical stability and require alternating current measurement to avoid the charging effect. Furthermore, they have relatively slow responses due to the ion transfer process.[12−15] On the other hand, liquid metals are promising materials due to their excellent electrical and thermophysical properties. As one of the liquid metallic materials, Galinstan has unique material properties such as self-healing capability, low melting point at around the room temperature, high electrical conductivity, and nontoxicity that make it highly promising for use in wearable soft electronic

Received: June 20, 2021
Accepted: August 7, 2021
Published: August 19, 2021



Downloaded via KOREA ADVANCED INST SCI AND TECHLGY on November 21, 2022 at 13:40:17 (UTC).
See https://pubs.acs.org/sharingguidelines for options on how to legitimately share published articles.

ACS Publications © 2021 American Chemical Society

devices. However, conventional liquid-metal-based pressure sensors have shown low pressure sensitivity, and thus, there have been some efforts to improve their sensitivity. Previous studies have utilized the triple state of liquid metal microchannels,[16] diaphragm pump structuring,[17] and internalization of rigid objects within the liquid metal channels.[18] In our previous study, we proposed the development of a liquid-metal-based pressure sensor by utilization of the multimaterial 3D printing method. The pressure sensitivity of the liquid-metal-based pressure sensor has increased by integration of a 3D-printed rigid microbump array onto the liquid metal channel.[19] However, in our previous study, a parametric study about the effect of dimensions of the rigid microbump on the liquid-metal-based pressure sensor was not conducted. Furthermore, there have been very few studies about the strategies to suppress the pressure sensitivity in the interconnection area of liquid-metal-based sensors for mechanically robust and stable wearable device integration.

In this study, we introduce a 3D-printed rigid microbump-array-integrated liquid-metal-based soft pressure sensor that features an optimization of the microbump dimensions and the integration of the optimized microbumps (E-bump and A-bump) into a fingertip pressure sensor. The structure of the proposed soft pressure sensor is constructed via multimaterial fused deposition modeling (FDM). The 3D-printed structure is divided into two different layers such as the water-soluble microchannel mold and rigid microbump arrays that are simultaneously embedded into the elastomer. Liquid metal channels are formed by sacrificing the water-soluble microchannel mold and then by filling the channels with the liquid metal. The rigid microbump arrays stand above the microchannels through the embedded structure between the microchannel and elastomer. Importantly, the current study demonstrates wide applications of the fingertip pressure sensor for wearable electronics based on liquid metal, which makes use of the increased sensitivity in the pressure-sensitive area by the E-bump. Moreover, the interconnections of the constructed sensors were not significantly affected by external stimuli, owing to the decreased pressure sensitivity by the A-bump. Herein, we illustrated the applications of the proposed fingertip pressure sensor in traditional East Asian medicine (TEAM) that can monitor the wrist pulsation by palpation. Furthermore, the proposed wearable fingertip pressure sensor was applied to remote controlling and the Flappy Bird game.

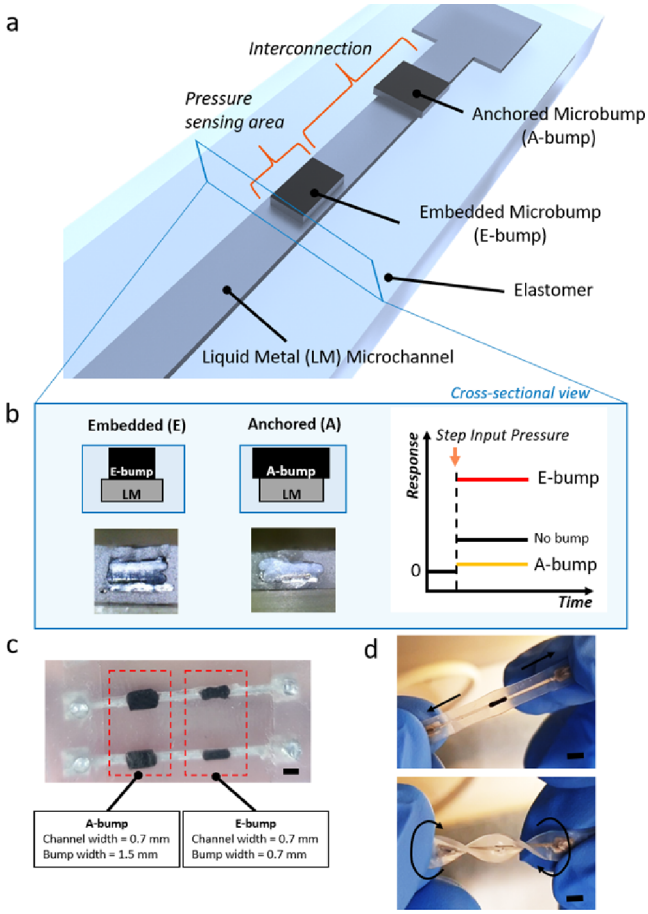


Figure 1. (a) Schematic design image of a 3D-printed A-bump- and E-bump-integrated liquid-metal-based pressure sensor. (b) Effect of the E-bump and A-bump on the pressure sensitivity. (c) Image of liquid metal microchannels integrated with E-bumps (right) and A-bumps (left) (scale bar = 3 mm). (d) Images of the single liquid metal microchannel with an E-bump bump under stretching and twisting (scale bar = 2 mm).

RESULTS AND DISCUSSION

Design and Fabrication. The 3D-printed rigid microbump-integrated liquid-metal-based soft pressure sensor is basically divided into four main parts: bottom layers, liquid metal channels, 3D-printed microbumps, and top layer. The detailed schematic of the sensor is presented in Figure 1a–c. The top and bottom layers of the sensor are made of Dragon Skin 10 with a low elastic modulus (E = 150 kPa for ε = 100%) and an extremely high stretchability (1000%). The excellent mechanical properties of Dragon Skin and liquid metal provide a perfect reversibility and robustness in stretching and twisting deformations (Figure 1d). Briefly, the 3D-printed rigid microbump-integrated liquid-metal-based soft pressure sensor is fabricated with a multinozzle FDM 3D printing process. The schematic of the fabrication processes can be found in Figure S1. There are two layers for 3D printing, which are polylactic acid (PLA) and polyvinyl alcohol (PVA). PVA is used as a sacrificial layer for the formation of a liquid-metal-based microchannel. On the other hand, PLA is used for the rigid microbump array formation. To fabricate the microchannels, the PVA layer is removed by water intrusion, while the rigid PLA microbumps are monolithically integrated onto the elastomer layer. Then, the microchannel is filled with Galinstan (Figure 1c). The electrical interconnection is made by embedding the electrical wires into the liquid-metal-filled microchannel. Finally, the 3D-printed rigid microbump-integrated liquid-metal-based soft pressure sensor is embedded onto a thimble-shaped elastomer (Figure S2).

Design of Pressure Sensitivity. When pressure is applied to the liquid metal microchannel, the cross-sectional area of the microchannel decreases and it leads to an increase in the electrical resistance of the microchannel. Under the application of a normal stress (σ_z), the change in the height of the microchannel (Δh) can be described using eq 1 and the relative change in the resistance can be represented using eq 2, which is based on the linear elastic fracture mechanics[20] (Figure S3a,b).

$$\Delta h = \frac{2(1-\nu^2)w\sigma_z}{E} \quad (1)$$

https://doi.org/10.1021/acsaelm.1c00546
ACS Appl. Electron. Mater. 2021, 3, 4027–4036

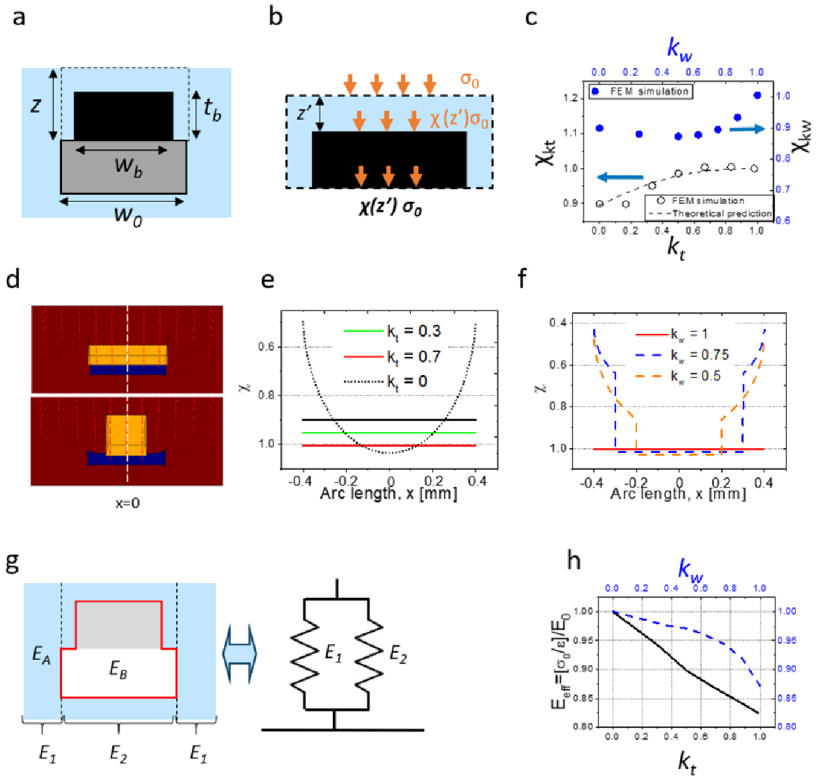


Figure 2. Working principle of the 3D-printed microbump-integrated liquid metal soft pressure sensor. (a) Geometry of the microbump-integrated liquid metal pressure sensor. k_t: thickness ratio of the microbump to top elastomer layer (t_b/z). k_w: width ratio of the microbump to liquid metal channel (w_b/w_0). (b,c) Effect of k_w and k_t on χ. When k_t and kw approach 1, χ also approaches 1, which is theoretically a complete transmission of pressure from the surface to the microchannel. (d) FEM simulation of the integration of the microbump. (e) χ vs arc length when k_w = 1. When k_t = 0, there is a parabolic distribution of χ with respect to the arc length (black dotted curve). Here, the black solid line represents the average χ value for the parabolically distributed χ values. However, when the microbump is integrated, there is a constant χ with an increased value across the arc length. (f) χ vs arc length when k_t = 0.7. Only the surface where the microbump exists has a constant value, and the other part shows a parabolic curve of χ. (g,h) Effect of k_w and k_t on E_{eff}. The black solid curve represents the change of E_{eff} by varying k_t while k_w is fixed at 0.5. The blue dashed curve represents the change of E_{eff} by varying k_w while k_t is fixed at 1. As k_t and k_w approach 1, E_{eff} decreases by more than 10%.

$$\frac{\Delta R}{R_0} = \left(\frac{1}{1 - \frac{2(1-\nu^2)}{E}\chi\sigma_z\left(\frac{w}{h}\right)} - 1 \right) \tag{2}$$

where w and h are the width and height of the microchannel, respectively, ν is Poisson's ratio, E is Young's modulus of the elastomer, and χ is the correction factor. When normal stress (σ_z) is applied on the surface of the elastomer, the magnitude of the stress decreases in the Z direction. The pressure applied to the top surface of the microchannel is diminished by the correction factor χ. According to the equation, to increase the relative resistance change, the change in the cross-sectional area of the microchannel should be increased, which is dependent on the transmitted pressure to the microchannel and the effective mechanical modulus of the structure. Accordingly, there are two strategies to increase the pressure sensitivity: (i) increasing the correction factor χ or (ii) decreasing the effective mechanical modulus of the structure. In previous studies,[20−22] researchers tried to change the effective mechanical modulus by changing the geometry of the microchannel (w/h). To investigate the geometric effect of the liquid metal pressure sensor, three parameters are defined (i.e., z: thickness of the top layer, h: height of the microchannel, and w: width of the microchannel) and the resistance change over the same applied pressure was calculated using finite element method (FEM) simulation (COMSOL) (Figure S3c). It is found that the pressure sensitivity is inversely proportional to the height of the microchannel and the thickness of the top layer and proportional to the width of the microchannel.

In our study, we found that the integration of a rigid microbump can increase the correction factor and decrease the mechanical modulus of the structure. The schematic view of the integrated microbump and microchannel geometry is shown in Figure 2a. We defined that k_t is the ratio of the thickness of the top elastomer (z) and thickness of the microbump (t_b) and k_w is the ratio of the width of the liquid metal microchannel (w_0) and the width of the microbump (w_b). When k_t is 1, the rigid microbump is totally covering the top surface of the microchannel, and when k_t is 0, there is no microbump. When k_w is 1, the width of the microbump and that of the microchannel are the same, and $k_w > 1$ means that the width of the microbump is larger than that of the microchannel, and vice versa.

First, when the microbump exists ($k_t > 0$), the rigid microbump helps the transmission of the applied stress from the top surface of the elastomer to the that of the microchannel. Since the rigid microbump, having an elastic modulus of 3.5 GPa, does not deform due to its high elastic modulus, it directly transmits the pressure applied on the top of the microbump to the bottom. It means that the correction factor χ is changed to $\chi = \chi(z - t_b) = \chi(z')$ by introducing the microbump. Thus, the integration of the rigid microbump

https://doi.org/10.1021/acsaelm.1c00546
ACS Appl. Electron. Mater. 2021, 3, 4027−4036

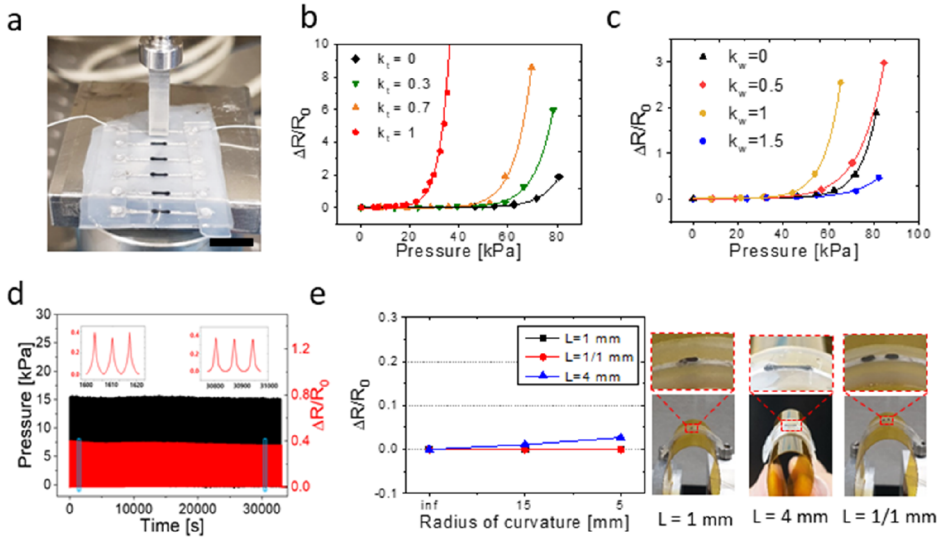


Figure 3. Design of the microbump with respect to the value of k_t and k_w. (a) Single microchannel sensor test for the evaluation of the effect of the microbump (scale bar = 10 mm). (b) Effect of k_t. When k_t approaches 1, the sensitivity significantly increases. (c) Effect of k_w. When k_w is below 1, there is an increase of the sensitivity by increasing k_w. When k_w is larger than 1, the A-bump prevents the deformation of the microchannel, decreasing the sensitivity. (d) 10,000 cyclic loadings with the repeating compressive pressure of 0−15 kPa. (e) Effect of the length of the microbump on bending. L = 1, 4, and 1/1 mm cases are experimentally observed. Negligible signal change was observed when L is 1 and 1/1 mm (i.e., two 1 mm long microbumps are integrated with a gap of 1 mm).

changes the effective thickness of the top elastomer from z to z' and increases the magnitude of the stress transmitted to the microchannel. Therefore, the pressure transmitted to the microbump can be established as $\chi(z')\sigma_z$ (Figure 2b). Theoretical prediction of χ is done by Boussinesq's method (Figure S4). When the correction factor χ is close to 1, almost complete transmission of the pressure from the top surface of the elastomer to the microchannel occurs. χ approaches 1 when k_t is above 0.6 and k_w is close to 1 (Figure 2c). It infers that, as k_w increases, the microbump covers more area of the microchannel and delivers more stress to the microchannel with higher correction factors. When the load is applied, the top surface profile of the microchannel is deformed, as shown in Figure 2d−f. The top surface of the microchannel without microbump has a parabolic curve according to the arc length (x). When a microbump with k_w = 1 is integrated, the surface profile becomes straight in the region in contact with the rigid microbump as there is no deformation in the rigid microbump (Figure 2e). When k_w is below 1, the top surface profile becomes a combination of a straight line at the center and a parabolic curve at the other areas. The average χ value appears at the descent below 0.5 and the ascent above 0.5 of k_w. Therefore, k_t should be close to 1 and k_w should be above 0.5 for the enhancement of pressure sensitivity (Figure 2f).

Second, the integration of the microbump can also increase the pressure sensitivity by decreasing the effective mechanical modulus of the composite structure. The liquid metal pressure sensor structure can be assumed as the composite structure composed of two different materials with different mechanical moduli (E_1: elastomer and E_2: elastomer + liquid metal). Because the pressure is applied on the top surface and incurs the same deflection of the material, effective modulus can be simply obtained using eq 3, where v_1 and v_2 are the volume fractions of materials 1 and 2, respectively. Furthermore, material 2 is a composite of materials A (elastomer) and B (liquid metal) with the same stress, which leads to the effective modulus as follows, where v_{2A} is the volume fraction of material A and v_{2B} is the volume fraction of material B (Figure 2g).

$$E_{\text{eff}} = E_1 v_1 + E_2 v_2 \tag{3}$$

$$E_2 = \frac{1}{\left(\frac{v_{2A}}{E_A} + \frac{v_{2B}}{E_B}\right)} \tag{4}$$

When the microbump is integrated into the microchannel, the volume fraction v_{2B} increases, leading to the decrease in E_2. Here, the elastic modulus of the rigid microbump is not considered because the interface between the microbump and the elastomer's inner surface is not chemically bonded but physically overhung. Although the friction or physical interaction at the interface would make a reduction in the decreasing ratio from the increase of v_{2B}, the effective modulus decreases as k_t and k_w increase (Figure 2h). This result could be supported by the FEM simulation result, showing that the cross-sectional area has further reduced when the rigid microbump is integrated into the microchannel under the same pressure (Figure S5).

The microbump could be classified into two types according to the width of the microbump (k_w): E-bump and A-bump. For an E-bump, k_w is equal to or less than 1, providing a stable and robust structure for the pressure sensor with a high-pressure sensitivity. For an A-bump, k_w is larger than 1, the width of the microbump exceeding that of the microchannel, which reduces the pressure sensitivity due to the A-bump on the sidewall of the liquid metal microchannel.

Although the correction factor χ is increased by increasing k_w, the A-bump prevents the microchannel from mechanical deformation by mechanical anchoring. To evaluate the performances of each microbump design, single channel liquid-metal-based pressure sensors with various microbump geometries were fabricated and characterized (Figure 3a). When k_t increased, the response significantly increased as compared to the conventional liquid metal pressure sensor without any microbump (k_t = 0). In particular, when k_t = 1, the

https://doi.org/10.1021/acsaelm.1c00546
ACS Appl. Electron. Mater. 2021, 3, 4027−4036

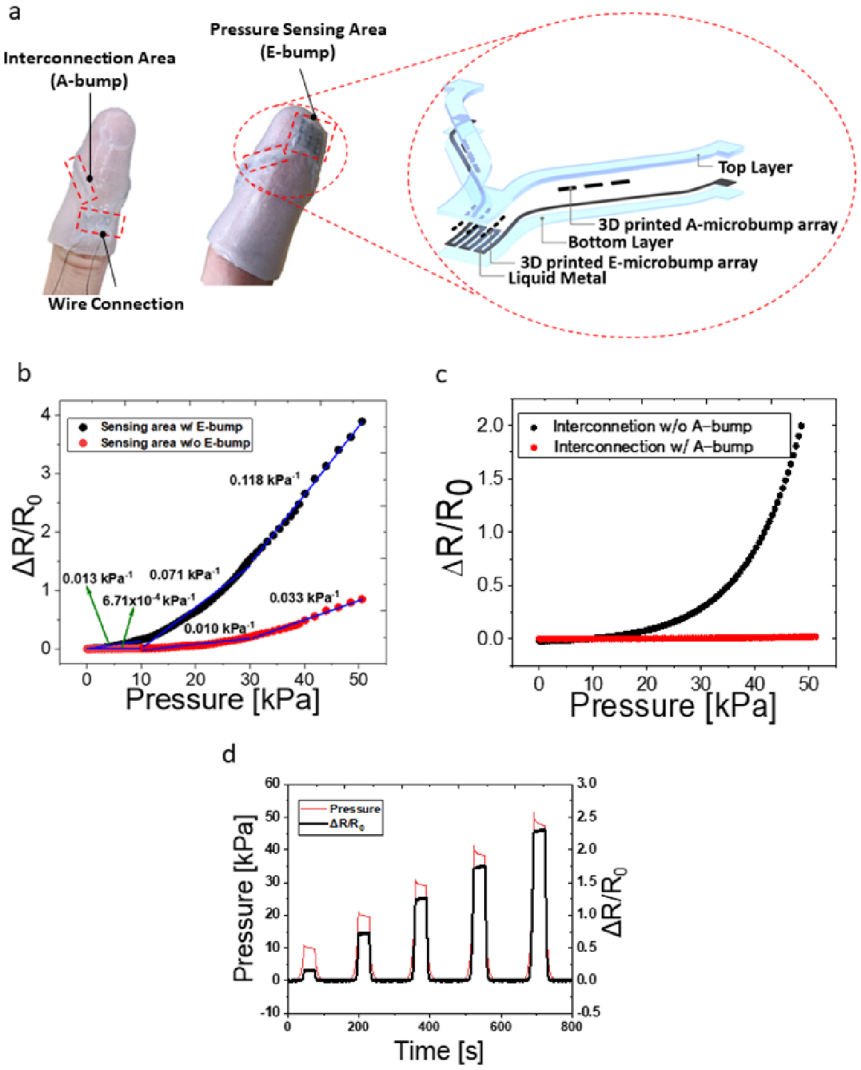


Figure 4. Structure and assessment of the fingertip pressure sensor. (a) Schematic view of the fingertip pressure sensor that is based on a 3D-printed rigid microbump-integrated liquid-metal-based pressure sensor. (b) Variation of the relative resistance with pressure and the sensitivity within ranges of 0−10, 10−30, and 30−50 kPa. (c) Relative resistance change of the interconnection area with/without anchored microbump under pressure. (d) Dynamic response of the sensor to varying pressure application.

sensor showed very high pressure sensitivity even in the low-pressure range (<30 kPa). Also, when k_w increased up to 1, the responses were enhanced compared to the liquid metal sensor without microbump. However, when k_w = 1.5, the A-bump inhibited the change in microchannel geometry, resulting in a reduced pressure sensitivity. Therefore, when an E-bump, which is a rigid microbump with k_w < 1, is integrated into the microchannel, the external pressure leads to a significant reduction in the cross-sectional area of the microchannel by locally concentrated deformation below the microbumps, while the correction factor increases and the effective modulus decreases. Consequently, the sensor response to the same applied pressure would be greatly improved by employing an E-bump (Figure 3b,c). In addition, under 10,000 cyclic loading with the repeated compressive pressure of 0−15 kPa, a long-term stability and mechanical durability of the sensor were observed (Figure 3d). In the 8th and 8960th cycle, the normalized resistances of change of the base lines are 0.00611 and 0.00636, respectively, with an increase of 4.1% only. The sensor showed a stable performance of measuring the pressure after 10,000 repetitive cycles. These results indicate that the sensor shows a good long-term stability. The bending test showed that when the length of microbump L is 1 mm (case I), the relative resistance change is negligible. When L is 4 mm (case II), the relative resistance increases to 0.027. Therefore, to reduce the effect of bending, multiple short microbumps with small gaps can be integrated instead of a single long microbump. The bending insensitivity is verified by the experimental result in which two 1 mm long microbumps are integrated with a gap of 1 mm (case III) (Figure 3e). To investigate the detection limit of the sensor, small pressures were applied to the sensing area from 0 to 660 Pa (Figure S6). The detection limit was evaluated as LOD = $\frac{3\sigma}{b}$, where σ is the standard deviation of the response and b is the slope of the calibration curve.[23] The detection limit of the sensor was calculated as 15 Pa. The sensitivity, detection range, and insensitive interconnection properties of the proposed sensor are comparable with the previously introduced liquid-metal-based pressure sensors and summarized in Table S1.

Integration of E-Bump and A-Bump into the Wearable and Wireless Liquid-Metal-Based Fingertip Pressure Sensor. To demonstrate a wide range of

https://doi.org/10.1021/acsaelm.1c00546
ACS Appl. Electron. Mater. 2021, 3, 4027−4036

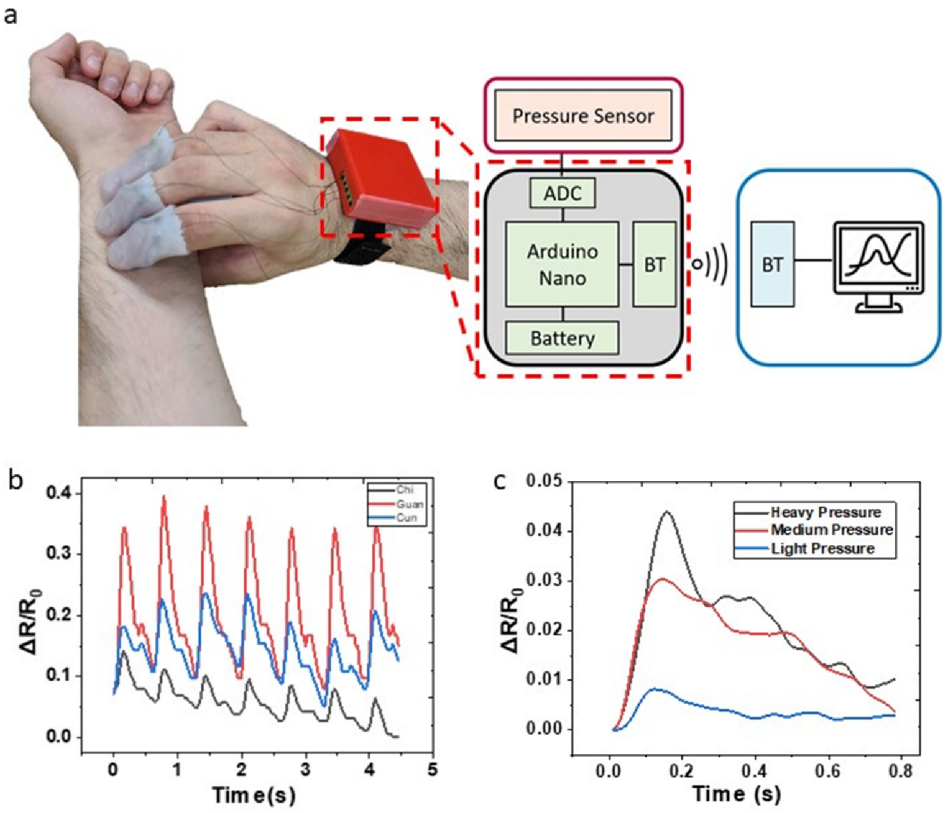


Figure 5. Application of the fingertip pressure sensor to pulse measurement in traditional East Asian medicine: (a) image of the measurement method of the fingertip pressure sensor and structure design of the data acquisition and wireless communication platform. (b) Wrist pulse waveforms of the test subject on the Chi, Guan, and Cun locations. (c) Single-region pulse wave measurement on the Guan position with different pressures.

applicability of the E-bump and A-bump structures, a wireless liquid-metal-based fingertip pressure sensor has been developed. The fingertip pressure sensor is composed of two parts: pressure sensing area and interconnections. The pressure sensing area has a serpentine pattern of microchannel, having an area of 10 × 10 mm^2. We designed k_t/k_w of the E-bump as 0.5/1.0 to enhance the pressure sensitivity of the sensor and that of the A-bump as 0.5/2.0 to minimize the pressure sensitivity. The dimensions of the E-bump and A-bump were 0.4 × 1 × 0.4 mm and 1.5 × 3 × 0.4 mm (width, length, and thickness), respectively. The pressure sensing area had a 3 × 4 E-bump array, and the interconnection area had a 1 × 3 A-bump array (Figure 4a). The geometry of the interconnection was designed to smoothly cover the finger when it is made into the form of a thimble. The length of the interconnection was designed as the end of the interconnection that could meet at the middle phalanx of the finger. The detailed fabrication process is demonstrated in Figure S2. The total length of the fingertip sensor was 40 mm, and the thickness was 1 mm. Figure 4b shows the experimental data of the relative resistance change of the fingertip pressures sensor with and without E-bumps. The pressure response test graph is divided into three different sections such as 0−10, 10−30, and 30−50 kPa. The correlation coefficients (R_2) are 0.961, 0.977, and 0.997 for each of these ranges, respectively. Meanwhile, the sensitivities are 0.013, 0.071, and 0.118 kPa^{-1} for each of these ranges, respectively. E-bump-integrated pressure sensor's average sensitivity is 0.0727 kPa^{-1}, and it is 5.43 times higher than that of the pressure sensor without E-bumps at the 0−50 kPa range. This can be attributed to the pressure sensitivity enhancement by the E-bump as explained above. On the other hand, the interconnection area is another essential part of the wearable devices for signal transmission. Previously developed liquid-metal-based sensors have not been equipped with special structures to prevent the effect of external stimuli on the interconnection area that cause distortion in the measured signal. In the present study, with the integration of A-bumps into the interconnection area, it is possible to achieve an excellent signal stability in the wearable device and to secure a high reliability in the pressure sensing data. As shown in Figure 4c, A-bump-integrated interconnection sensitivity is 0.0004 Pa^{-1} in the range of 0−50 kPa, which is 91.65 times lower than that of the pressure sensor with any microbumps. Figure 4d shows the reversible sensor response to dynamic loading at varying pressures. In the case of Figure 3b, we conducted the experiment with a single microbump structured sensor that can be referred in Figure 3a. The single-microbump-structured sensor length is shorter (20 mm) than that of the fingertip pressure sensor (138 mm), which can be referred in Figure 4a. Therefore, the total resistance was larger for the wearable fingertip pressure sensor than for the single-microbump-structured sensor in Figure 3a. As a result, the increase in the base resistance (R_0) of the sensor reduced the response ($\Delta R/R_0$) of the sensor.

Potential Applications of the Fingertip Pressure Sensor. *Application 1: Pulse Measurement in TEAM.* Identification of the health status and diagnosis of disease through pulse palpation have been carried out in TEAM for a long time. Pulse palpation is one of the four major examinations in TEAM. TEAM doctors use pulse palpation

https://doi.org/10.1021/acsaelm.1c00546
ACS Appl. Electron. Mater. 2021, 3, 4027−4036

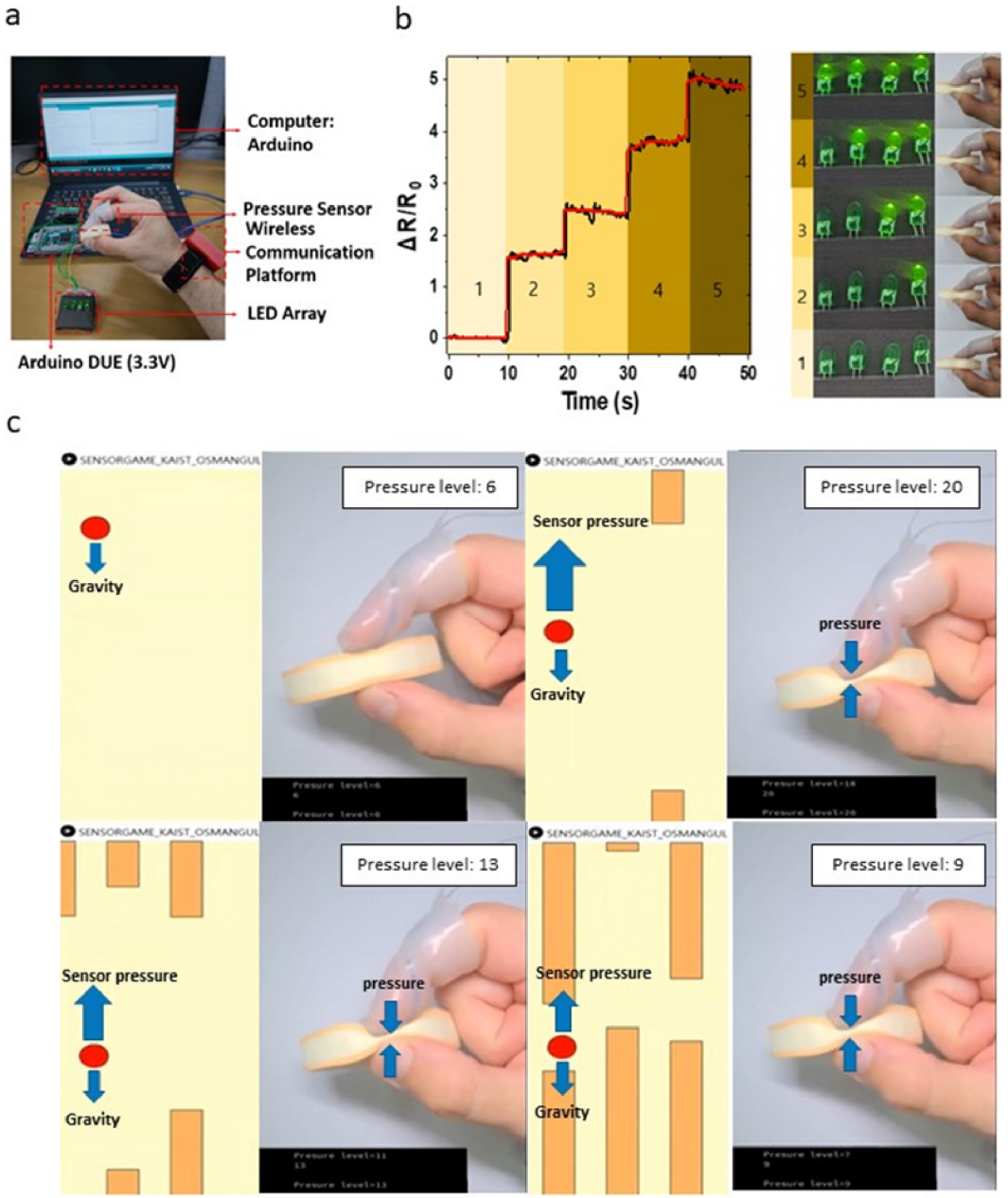


Figure 6. Application of the fingertip pressure sensor to the human−machine interface. (a) Relative resistance change response to the applied pressure for remote controlling of an LED array. (b) Output as LED turn on−off and light brightness corresponding to the applied pressure. (c) Images of the Flappy Bird game application. Gravity is applied to the bird that pushes it toward the ground, and the applied pressure lifts the bird upward against the gravity.

at three locations (Cun, Guan, and Chi) on both wrists to check up the health conditions of the patients and specific organ conditions.[23,24] The pulse measurement has two classifications. First, the pulse is measured at a single position, specifically in Guan. Second, the pulse is measured in three positions (Cun, Guan, and Chi), which depends on the theory of three positions and nine indicators (TPNI). TEAM doctors go through an experience-based education program to make the medical assessments by applying different pressures and processing the pulse measurement at the three locations without instruments. Recently, researchers have made various attempts to prove the identification of the health condition and diagnosis of a disease scientifically through quantitative pulse measurement systems.[25−29] However, previously developed systems did not allow the TEAM doctors to get involved in the pulse measurement process. In other words, the measurements were made by attachment of sensors directly on the human wrist or on the mechanical measurement devices; therefore, the TEAM doctors could not sense the wrist pulse during the measurement period.

However, there is a strong demand from TEAM doctors on the wearable pulse measurement systems that they can wear on their fingers to apply various pressures on the human wrist for acquisition of different pulse palpation patterns according to TPNI theory. Therefore, the present work has proposed a wireless and wearable soft fingertip pressure sensor that highly interacts with TEAM doctors on pulse palpation. It is lightweight, easy to operate, and convenient in pulse

https://doi.org/10.1021/acsaelm.1c00546
ACS Appl. Electron. Mater. 2021, 3, 4027−4036

measurement to identify health status and to diagnose the diseases. Figure 5a shows the schematic of a three-finger palpation measurement system for data acquisition and wireless data communication. The detailed schematic information is described in the Experimental Section and demonstrated in Figure S7. Figure 5b shows three-finger palpation results in Chi, Cun, and Guan locations. The Guan location shows the largest $\Delta R/R_0$, followed by Cun and then Chi positions. Figure 5c shows the single-region measurement of the pulse pattern under light pressure, medium pressure, and heavy pressure on the Guan location (Video S1). These results show that the proposed fingertip pressure sensor can be easily utilized by TEAM doctors to analyze the patient's wrist pulse wave. Although the patient is the same, different doctors sense the wrist pulse waves and analyze them differently. Therefore, the proposed device will help improve the analysis of the wrist pulse wave and obtain more reliable data. In contrast to the previously proposed devices, the proposed device gives a chance to sense the patience wrist pulse directly while the doctor wears the device due to the soft properties of the device. This will be beneficial for the TEAM doctors in two ways. First, the trainee doctors will easily learn and understand how to sense and analyze the wrist pulse waveforms with real-time visualization of the wrist pulse while they sense the wrist pulse waveforms by palpation. Second, with the reliable data recorded from the device, the doctors will have an opportunity to match the sensation results and real-time pulse waveforms to diagnose the patients more accurately.

Application 2: Human–Machine Interface. We demonstrated remote control of an LED array and the Flappy Bird game to verify the possible applications of the human–machine interface (HMI) using the proposed wearable fingertip pressure sensor, as shown in Figure 6. Figure 6a–c shows the applications of the fingertip pressure sensor on the LED light brightness. The detailed schematic of the wireless communication system of the fingertip pressure sensor and LED illumination setup is illustrated in Figures 6a and S8. Figure 6b shows a relative resistance change by a gradual increase of the applied pressure for remote controlling of LED. Here, it is demonstrated that the brightness of the LEDs increases depending on the applied pressure level. Nowadays, wearable devices are utilized for entertainment purposes and they have a superior user satisfaction rate. To demonstrate the high potential applicability of our wearable fingertip pressure sensor in entertainment systems, we used the fingertip pressure sensor to play the Flappy Bird game. The gravity is applied to the bird, and the location of the bird is adjusted with the pressure measured by the fingertip pressure sensor, as shown in Figures 6c and S9 (Video S2). The pressure sensor is able to detect small pressures applied by the fingertip and move the bird upward according to the applied pressure, which demonstrates a useful application of the proposed wearable sensor to the entertainment system.

CONCLUSIONS

In the present work, we have introduced a pressure-sensitivity-controllable soft liquid-metal-based pressure sensor assisted by 3D-printed microbumps to resolve the problems of low-pressure sensitivity and unstable interconnection of the conventional liquid–metal-based soft pressure sensors reported in the literature. We investigated the controllability of the pressure sensitivity depending on the microbump dimensions and optimized two microbump configurations (E-bump and A-bump) for a wearable pressure sensor application. The E-bumps are useful if the pressure sensitive area of the liquid-metal-based pressure sensor needs to have a high-pressure sensitivity. Conversely, in the interconnection area, which needs to have relatively low-pressure sensitivity and high signal stability against external stimuli, the A-bumps are utilized. Specifically, the E-bump structure increases the average sensitivity of the liquid metal channels by 5.43 times (0.0727 kPa^{-1}), and the A-bump structure decreases the average sensitivity by 91.65 times (0.0004 Pa^{-1}) in the range of 0–50 kPa.

Making use of the advantages provided by the E-bumps and A-bumps (for the specific purposes), we integrated them to construct a fingertip pressure sensor for two different wearable sensing applications: (1) a wearable three-fingertip pulse palpation device to help TEAM doctors measure and collect data related to the pulse patterns from the Cun, Guan, and Chi positions of a human wrist and (2) a wearable fingertip pressure sensor for the HMI. The proposed fingertip pressure sensor will provide many different opportunities with reliable data acquisition for TEAM doctors to analyze wrist pulse waves. On the other hand, the fingertip pressure sensor can be utilized in the wearable gaming platforms with high user-friendliness. The proposed approach to control the pressure sensitivity of the liquid-metal-based pressure sensor using different rigid microbump designs will be a very useful and versatile strategy for improving the performance and stability of many liquid-metal-based wearable devices.

EXPERIMENTAL SECTION

Materials. Dragon Skin 10 (Smooth-On, USA), Easy Release 200 (Smooth-On, USA), Ecoflex00-35 (Smooth-On, USA), Alja-Safe (Smooth-On, USA), Hydrocal (Smooth-On, USA), PVA filament (2.75 mm, Ultimaker, USA), PLA filament (2.75 mm, Ultimaker, USA), and Galinstan (Santech Materials, China) were all used as purchased.

Preparation of the 3D-Printed Mold. Microchannel molds were designed with the 3D CAD program (Fusion 360, Autodesk, USA). The width of the microchannel was designed as 0.7 mm, and the gap between the microchannels at the sensing region was 0.7 mm. The thickness of the sensing region was 0.2 mm and that of the electrode was also 0.2 mm (Figure S2). The dimensions of the E-bump and A-bump were 0.4 × 1 × 0.4 and 1.5 × 3 × 0.4 mm (width, length, thickness), respectively. After the modeling, the 3D CAD file was exported as an STL file for 3D printing and loaded in the 3D printing software program (Cura 3.2, Ultimaker, USA). The microchannel molds were 3D-printed using a commercial FDM 3D printer (Ultimaker 3, Ultimaker, USA) having a dual extrusion system. The molds were 3D-printed with customized printing conditions. After printing, the molds were carefully detached from the printing bed.

Fabrication of the Fingertip Pressure Sensor: *Sensor Fabrication Process.* Before spin coating, the release agent was coated on the glass wafer for easy release of the elastomer. The prepolymer mixture of Dragon Skin 10 was prepared by mixing its components, A and B, with a ratio of 1:1 and spin-coated (400 rpm, 60 s) on the prepared wafer as the bottom layer, followed by degassing in the vacuum chamber and curing at 60 °C. Then, the microchannel molds were put on the bottom layer and the additional prepolymer was spin-coated (250 rpm, 60 s) above them as the top layer, followed by degassing. After curing, small holes were generated at the end of the molds for PVA removal. Deionized water at 60 °C was used for consecutive water intrusion into the channel by a syringe, and then, the empty microchannel structure was fabricated. Then, the fabricated microchannel was filled with Galinstan by the vacuum filling method[30] or syringe injection. Afterward, the holes were sealed

https://doi.org/10.1021/acsaelm.1c00546
ACS Appl. Electron. Mater. 2021, 3, 4027–4036

with additional elastomer. The next step is the integration of the pressure sensor to the fingertip.

Fingertip Glove Integration Process. To integrate the pressure sensor to the fingertip glove, hand-shaped bulk mold is needed to prepare by molding and casting process. The hand was immersed into Alja-Safe, which was mixed with water, and allowed to cure for 10 min. Once Alja-Safe was set to a firm solid gel, the hand was carefully removed from the mold. Alja-Safe perfectly captured the hand shape and the mold was ready for the casting process. Hydrocal was dispensed into containers with mix ratio of 2-parts plaster: 1-part water by volume and mixed. Hydrocal was slowly sifted into the water. The water absorbed the powders for 2 min before stirring. Hydrocal and water were mixed for a minimum of 4 min, and the cavity was filled with the liquid Hydrocal, followed by curing for an hour at room temperature. The prepared pressure sensor was attached to the finger of the hand mold with a glue stick. After the placement, Dragon Skin 10 was poured onto the pressure sensor and cured at 60 °C for 10 min.

Sensor Characterization. To measure the cyclic response and pressure response of the sensor, a micro-actuator (MA-35, Physik Instrumente, Germany) and a force transducer (SM-500N, Interface, USA) were used under displacement control loading conditions.

Wireless TEAM Wrist Blood Pressure Monitoring, Game Controlling, and Remote Controlling System. The sensor and the reference resistor were connected in series for a voltage dividing circuit (Figure S5a). The regarded application system was divided into two parts: wireless communication platform and computer. The wireless communication platform consisted of ADS1115 (Texas Instruments, USA), Arduino Nano (Arduino.cc), Li−Po battery (Shenzhen Taiwoo Battery Co., Ltd, China), and HC-06 Bluetooth module (Arduino.cc). The fabricated fingertip pressure sensor was connected to the ADS1115 converter, which provided a 16-bit precision at 860 samples/s over I2C. The amplified signals were recorded by Arduino Nano. The power of the system was supplied by a Li-Po battery. The wireless communication of the system was constructed with the HC-06 Bluetooth module. The signals were delivered to the computer by the wireless communication platform and received by the oscillator program in a computer. The fingertip pressure sensors were worn on the fingers and then placed on the Cun, Guan, and Chi areas to measure the wrist pulse of the three different areas simultaneously for TEAM wrist pulse monitoring. The acquired ADC data were plotted and recorded in real-time by a serial oscilloscope program. The second application of the fingertip pressure sensor was remote controlling of the LED array. The signals acquired from the wireless communication platform were received by Arduino Due that remotely controlled the LED array. The third application of the fingertip pressure sensor was game controlling. The game programming of the game controlling system was done in the Processing program (processing.org, USA). The game principle is that the bird flies, its longitude is controlled depending on the applied pressure level, and the bird passes through to the walls. Also, gravity is applied in the game. The pressure sensor signal acquired from the wireless communication platform was received by the computer and used for the game control.

■ ASSOCIATED CONTENT

Supporting Information

The Supporting Information is available free of charge at https://pubs.acs.org/doi/10.1021/acsaelm.1c00546.

Schematic of the fabrication process of the pressure sensor, images of the fingertip pressure sensor for each of the fabrication steps, sensing mechanism of the liquid metal pressure sensor, modeling and simulation of the 3D-printed microbump-integrated pressure sensor structure, wireless pulse-monitoring system, wireless LED remote-controlling system, and wireless game system (PDF)

Movie S1, wireless flappy bird game playing with the fingertip pressure sensor (AVI)

Movie S2, wireless wrist pulse measurement system (AVI)

■ AUTHOR INFORMATION

Corresponding Author

Inkyu Park − *Department of Mechanical Engineering, Korea Advanced Institute of Science and Technology (KAIST), Daejeon 34141, South Korea;* orcid.org/0000-0001-5761-7739; Email: inkyu@kaist.ac.kr

Authors

Osman Gul − *Department of Mechanical Engineering, Korea Advanced Institute of Science and Technology (KAIST), Daejeon 34141, South Korea;* orcid.org/0000-0002-1972-7838

Kyuyoung Kim − *Department of Mechanical Engineering, Korea Advanced Institute of Science and Technology (KAIST), Daejeon 34141, South Korea*

Jimin Gu − *Department of Mechanical Engineering, Korea Advanced Institute of Science and Technology (KAIST), Daejeon 34141, South Korea*

Jungrak Choi − *Department of Mechanical Engineering, Korea Advanced Institute of Science and Technology (KAIST), Daejeon 34141, South Korea*

Dionisio Del Orbe Henriquez − *Department of Mechanical Engineering, Korea Advanced Institute of Science and Technology (KAIST), Daejeon 34141, South Korea;* orcid.org/0000-0002-1528-673X

Junseong Ahn − *Department of Mechanical Engineering, Korea Advanced Institute of Science and Technology (KAIST), Daejeon 34141, South Korea;* orcid.org/0000-0002-4090-5440

Complete contact information is available at: https://pubs.acs.org/10.1021/acsaelm.1c00546

Author Contributions

#O.G. and K.K. contributed equally to this work.

Notes

The authors declare no competing financial interest.

■ ACKNOWLEDGMENTS

This work was supported by a National Research Foundation of Korea (NRF) grant funded by the Korean government (MSIT) (no. 2021R1A2C3008742).

■ REFERENCES

(1) Boland, C. S.; Khan, U.; Backes, C.; O'Neill, A.; McCauley, J.; Duane, S.; Shanker, R.; Liu, Y.; Jurewicz, I.; Dalton, A. B. Sensitive, high-strain, high-rate bodily motion sensors based on graphene−rubber composites. *ACS Nano* **2014**, *8*, 8819−8830.

(2) Wang, Y.; Wang, L.; Yang, T.; Li, X.; Zang, X.; Zhu, M.; Wang, K.; Wu, D.; Zhu, H. Wearable and highly sensitive graphene strain sensors for human motion monitoring. *Adv. Funct. Mater.* **2014**, *24*, 4666−4670.

(3) Wang, Y.; Yang, R.; Shi, Z.; Zhang, L.; Shi, D.; Wang, E.; Zhang, G. Super-elastic graphene ripples for flexible strain sensors. *ACS Nano* **2011**, *5*, 3645−3650.

(4) Yan, C.; Wang, J.; Kang, W.; Cui, M.; Wang, X.; Foo, C. Y.; Chee, K. J.; Lee, P. S. Highly stretchable piezoresistive graphene−nanocellulose nanopaper for strain sensors. *Adv. Mater.* **2014**, *26*, 2022−2027.

(5) Kong, J.-H.; Jang, N.-S.; Kim, S.-H.; Kim, J.-M. Simple and rapid micropatterning of conductive carbon composites and its application to elastic strain sensors. *Carbon* **2014**, *77*, 199−207.
(6) Lu, N.; Lu, C.; Yang, S.; Rogers, J. Highly sensitive skin-mountable strain gauges based entirely on elastomers. *Adv. Funct. Mater.* **2012**, *22*, 4044−4050.
(7) Mattmann, C.; Clemens, F.; Tröster, G. Sensor for measuring strain in textile. *Sensors* **2008**, *8*, 3719−3732.
(8) Amjadi, M.; Pichitpajongkit, A.; Lee, S.; Ryu, S.; Park, I. Highly stretchable and sensitive strain sensor based on silver nanowire−elastomer nanocomposite. *ACS Nano* **2014**, *8*, 5154−5163.
(9) Xiao, X.; Yuan, L.; Zhong, J.; Ding, T.; Liu, Y.; Cai, Z.; Rong, Y.; Han, H.; Zhou, J.; Wang, Z. L. High-strain sensors based on ZnO nanowire/polystyrene hybridized flexible films. *Adv. Mater.* **2011**, *23*, 5440−5444.
(10) Kang, D.; Pikhitsa, P. V.; Choi, Y. W.; Lee, C.; Shin, S. S.; Piao, L.; Park, B.; Suh, K.-Y.; Kim, T.-I.; Choi, M. Ultrasensitive mechanical crack-based sensor inspired by the spider sensory system. *Nature* **2014**, *516*, 222−226.
(11) Lee, J.; Kim, S.; Lee, J.; Yang, D.; Park, B. C.; Ryu, S.; Park, I. A stretchable strain sensor based on a metal nanoparticle thin film for human motion detection. *Nanoscale* **2014**, *6*, 11932−11939.
(12) Yang, X.; Wang, Y.; Qing, X. A flexible capacitive pressure sensor based on ionic liquid. *Sensors* **2018**, *18*, 2395.
(13) Cho, S. H.; Lee, S. W.; Yu, S.; Kim, H.; Chang, S.; Kang, D.; Hwang, I.; Kang, H. S.; Jeong, B.; Kim, E. H. Micropatterned pyramidal ionic gels for sensing broad-range pressures with high sensitivity. *ACS Appl. Mater. Interfaces* **2017**, *9*, 10128−10135.
(14) Wang, Z.; Si, Y.; Zhao, C.; Yu, D.; Wang, W.; Sun, G. Flexible and Washable Poly (Ionic Liquid) Nanofibrous Membrane with Moisture Proof Pressure Sensing for Real-Life Wearable Electronics. *ACS Appl. Mater. Interfaces* **2019**, *11*, 27200−27209.
(15) Zhang, S.; Wang, F.; Peng, H.; Yan, J.; Pan, G. Flexible highly sensitive pressure sensor based on ionic liquid gel film. *ACS Omega* **2018**, *3*, 3014−3021.
(16) Yeo, J. C.; Yu, J.; Loh, K. P.; Wang, Z.; Lim, C. T. Triple-state liquid-based microfluidic tactile sensor with high flexibility, durability, and sensitivity. *ACS Sens.* **2016**, *1*, 543−551.
(17) Gao, Y.; Ota, H.; Schaler, E. W.; Chen, K.; Zhao, A.; Gao, W.; Fahad, H. M.; Leng, Y.; Zheng, A.; Xiong, F. Wearable microfluidic diaphragm pressure sensor for health and tactile touch monitoring. *Adv. Mater.* **2017**, *29*, No. 1701985.
(18) Shin, H.-S.; Ryu, J.; Majidi, C.; Park, Y.-L. Enhanced performance of microfluidic soft pressure sensors with embedded solid microspheres. *J. Micromech. Microeng.* **2016**, *26*, No. 025011.
(19) Kim, K.; Choi, J.; Jeong, Y.; Cho, I.; Kim, M.; Kim, S.; Oh, Y.; Park, I. Highly Sensitive and Wearable Liquid Metal-Based Pressure Sensor for Health Monitoring Applications: Integration of a 3D-Printed Microbump Array with the Microchannel. *Adv. Healthcare Mater.* **2019**, *8*, No. 1900978.
(20) Park, Y.-L.; Majidi, C.; Kramer, R.; Bérard, P.; Wood, R. J. Hyperelastic pressure sensing with a liquid-embedded elastomer. *J. Micromech. Microeng.* **2010**, *20*, No. 125029.
(21) Park, Y.-L.; Tepayotl-Ramirez, D.; Wood, R. J.; Majidi, C. Influence of cross-sectional geometry on the sensitivity and hysteresis of liquid-phase electronic pressure sensors. *Appl. Phys. Lett.* **2012**, *101*, No. 191904.
(22) Vogt, D. M.; Park, Y.-L.; Wood, R. J. Design and characterization of a soft multi-axis force sensor using embedded microfluidic channels. *IEEE Sens. J.* **2013**, *13*, 4056−4064.
(23) Shrivastava, A.; Gupta, V. B. Methods for the determination of limit of detection and limit of quantitation of the analytical methods. *Chron. Young Sci.* **2011**, *2*, 21−25.
(24) Tang, A. C. Y. Review of traditional Chinese medicine pulse diagnosis quantification. In *Complementary Therapies for the Contemporary Healthcare*, InTechOpen Limited, 2012; pp 61−80.
(25) Chu, Y.; Zhong, J.; Liu, H.; Ma, Y.; Liu, N.; Song, Y.; Liang, J.; Shao, Z.; Sun, Y.; Dong, Y. Human pulse diagnosis for medical assessments using a wearable piezoelectret sensing system. *Adv. Funct. Mater.* **2018**, *28*, No. 1803413.
(26) Jin, C.; Xia, C.; Zhang, S.; Wang, L.; Wang, Y.; Yan, H. A wearable combined wrist pulse measurement system using airbags for pressurization. *Sensors* **2019**, *19*, No. 386.
(27) Kabigting, J. E.; Chen, A. D.; Chang, E. J.-H.; Lee, W.-N.; Roberts, R. C. MEMS pressure sensor array wearable for traditional Chinese medicine pulse-taking. In *2017 IEEE 14th International Conference on Wearable and Implantable Body Sensor Networks (BSN)*; IEEE, 2017; pp 59−62.
(28) Luo, C.-H.; Chung, Y.-F.; Hu, C.-S.; Yeh, C.-C.; Si, X.-C.; Feng, D.-H.; Lee, Y.-C.; Huang, S.-I.; Yeh, S.-M.; Liang, C.-H. Possibility of quantifying TCM finger-reading sensations: I. Bi-sensing pulse diagnosis instrument. *Eur. J. Integr. Med.* **2012**, *4*, e255−e262.
(29) Wang, P.; Zuo, W.; Zhang, H.; Zhang, D. Design and implementation of a multi-channel pulse signal acquisition system. In *2012 5th International Conference on BioMedical Engineering and Informatics*; IEEE, 2012; pp 1063−1067.
(30) Lin, Y.; Gordon, O.; Khan, M. R.; Vasquez, N.; Genzer, J.; Dickey, M. D. Vacuum filling of complex microchannels with liquid metal. *Lab Chip* **2017**, *17*, 3043−3050.

https://doi.org/10.1021/acsaelm.1c00546
ACS Appl. Electron. Mater. 2021, 3, 4027−4036